

# Resolving the line-of-sight structure of galaxy clusters by combining X-ray and lensing data

Matthias Bartelmann<sup>1\*</sup> and Tsafrir S. Kolatt<sup>2,3†</sup>

<sup>1</sup> *Max-Planck-Institut für Astrophysik, P.O. Box 1523, D-85740 Garching, Germany*

<sup>2</sup> *Harvard-Smithsonian Center for Astrophysics, 60 Garden St., Cambridge, MA 02138, U.S.A.*

<sup>3</sup> *The Physics Department and Lick Observatory, University of California, Santa Cruz, CA 95064, U.S.A.*

1 February 2008

## ABSTRACT

The projected gravitational potential of galaxy clusters is reflected in both their X-ray emission and their imprint on the images of background sources due to their gravitational lensing effects. Since these projections of the potential are weighted differently along the line-of-sight, we propose a method to combine them and remove the degeneracy between two cases: (i) a cluster consisting of a single potential well, or (ii) an apparent cluster composed of several potential wells projected onto each other. We demonstrate with simulated data of potential models that this method indeed allows to significantly distinguish multiple from single clusters. The confidence limit for this distinction depends on the mass ratio between the clusters. It ranges from  $\sim 15\sigma$  for mass ratio 1:1 to  $\sim 4\sigma$  for mass ratio 1:6. Furthermore, the method reconstructs the correct cluster mass, the correct mass ratio of the two clusters, and the correct scale radii with typical fractional accuracies of a few percent at  $3\sigma$  confidence. As an aside, our method allows to accurately determine gas fractions in clusters, also with  $3\sigma$  fractional accuracies of order a few percent. We argue that our method provides an alternative to the commonly used  $\beta$ -fit technique, and yields more reliable results in a broader range of cases.

**Key words:** galaxies: clusters: general — cosmology: gravitational lensing — X-ray: General — methods: statistical

## 1 INTRODUCTION

What physical objects do we call galaxy clusters? Are they typical large regions of extreme density enhancement? Or do they, as a class, constitute a sample of peaks in the apparent, line-of-sight projected density of galaxies, X-ray emission, or dark matter? If so, what do cluster samples defined by different criteria have in common? Are the estimates of cluster abundance, and the inferences on cluster properties, misleading because of projection effects? What are our chances to identify and quantify projection effects?

The paramount importance of galaxy clusters as probes for the cosmological evolution of density perturbations and structure formation makes the answers to these questions essential for any attempts at interpreting cluster samples.

Despite their undoubted merits, cluster samples compiled by subjective classification of two-dimensional galaxy-count enhancements (Abell 1958; Zwicky *et al.* 1968; Abell,

Corwin, & Olowin 1989) are most susceptible to being statistically unfair. Identifying clusters by counting galaxies in an automated process (*e.g.* Dalton *et al.* 1994) marks a major improvement, but the so-defined samples are still subject to projection effects.

The prevalence of projection effects is reduced in cluster samples selected by X-ray surface brightness (*e.g.* Gioia *et al.* 1990; Ebeling *et al.* 1996). Arising mostly from thermal *bremsstrahlung*, the X-ray emissivity is proportional to the squared electron density in the intracluster plasma. It is therefore a much more reliable measure of the three-dimensional rather than the projected density. Despite this welcome feature, there is still ample room for selection effects to be important in some of the analyses based on such samples.

Recently, van Haarlem, Frenk, & White (1997) demonstrated with simulations that projection effects are important even for cluster samples selected by X-ray emission. The line-of-sight integrated X-ray emission of these clusters is usually fitted with the three-parameter  $\beta$  model (Cavaliere & Fusco-Femiano 1976). Unfortunately, conclusions from such fits suffer from projection effects and noise, and

\* e-mail: mbarthelmann@mpa-garching.mpg.de

† e-mail: tsafrir@physics.ucsc.edu

usually cease to provide an adequate functional description of the dark-matter density profile on intermediate scales of projected radii.

Our ability to recover the line-of-sight (l.o.s.) density structure is crucial for attempts at constraining cosmological parameters from cluster samples. It is also vitally important for any assessment of the physical properties of clusters, *e.g.* the degree of virialization and of hydrostatic equilibrium of the intracluster gas. For example, when rich clusters are selected for their strong gravitational lensing effects (*i.e.* their ability to form large arcs), and then analyzed with respect to their X-ray data to derive limits on the justification of the assumption of hydrostatic equilibrium (Miralda-Escudé & Babul 1995; Loeb & Mao 1994), it may well be that selection effects play an important role, and that some of the conclusions can be relaxed by taking projection effects into account (Bartelmann & Steinmetz 1996).

Another important application concerns the use of the Sunyaev–Zel’dovich effect (*e.g.* Sunyaev & Zel’dovich 1980; Rephaeli 1995). The effect can be used in two alternative ways. First, we can assume the line-of-sight extent of the cluster gaseous component (*e.g.* by relating it to the angular size using a Hubble constant). Then, by examining the distortion of the CMB spectrum, we can get limits for the gas content of the cluster and its temperature. On the other hand, we can assume the latter two (or estimate them differently) and deduce the Hubble constant by the comparison of the angular and line-of-sight extent. In either case, the result depends strongly on the true l.o.s. gas profile. If the latter is not well known, neither the Hubble constant nor the gas content can reliably be determined (see, *e.g.*, Roettiger *et al.* 1997; Holzappel *et al.* 1997).

Turning to clusters as tracers of the large-scale structure, we are facing the same problem again. Knowledge of the l.o.s. cluster profile is important for attempts at deriving the cluster abundance (White, Efstathiou, & Frenk 1993; Eke, Cole, & Frenk 1996; Viana & Liddle 1996), the cluster mass function (*e.g.* Bahcall & Cen 1993; Burns *et al.* 1996), the spatial distribution of clusters (*i.e.* correlations, probability distributions etc., see Bahcall 1988 for a review), and the cluster velocity dispersion (*e.g.* Fadda *et al.* 1996; Mazure *et al.* 1996).

In this paper, we propose an alternative to the traditional  $\beta$ -fit analysis and argue that, at least to some extent, degeneracies due to projection effects can be broken. The proposed alternative rests on a simple idea. In hydrostatic equilibrium, it must be possible to describe with the same gravitational potential all observable X-ray and lensing data pertaining to a given cluster. The specific relation between the potential and the X-ray emission depends on the equation of state and the temperature structure of the gas. It is sufficient to fix these two (and the connection between the dark matter and spatial gas distribution) in order for the method to work. Other assumptions do not affect the principle of our approach.

The available observational data are (i) the line-of-sight integrated X-ray flux, (ii) the emission-weighted gas temperature, and (iii) the gravitational lensing effects of the cluster that give rise to, *e.g.*, coherent distortions of the images of background sources. It is especially the combination of X-ray and lensing measurements that promises to break the degeneracies arising from projection effects. In particular, the X-

ray flux is most sensitive to the gas fraction and the physical extent of the system along the line-of-sight. The emission-weighted temperature is most sensitive to the depth of the three-dimensional potential well, and the shear field is most sensitive to the integrated gravitational potential (with the nice feature of being indifferent to the gas content).

For the sake of demonstration, we investigate two classes of three-dimensional potentials: (i) a single, isolated cluster, and (ii) two well separated clusters projected onto each other along the line-of-sight. In both cases, we describe the intracluster plasma as an isothermal ideal gas with spatially constant mean molecular weight. Fixing the functional form of the gravitational potential, we simulate “observed” X-ray flux maps, X-ray spectra, and lensing distortion maps. Given these synthetic observations, we search the parameter space of this functional form. We minimize an appropriate  $\chi^2$  function which contains contributions from all three types of data. As we shall show, the best-fit model parameters reproduce the input potential very reliably. Moreover, the degeneracy between the one- and two-cluster solutions is removed. Attempts to fit a functional form different from the one simulated result in a very poor goodness-of-fit relative to the goodness-of-fit for the correct functional form.

We start (§2) by specifying the explicit and implicit assumptions we make and provide a concise description of the observations. We proceed by relating the observables to the underlying gravitational potential (§2). In the same section, we present the functional form of the potential we choose. The combination of all observables, and the models to describe them, allows us to write down a  $\chi^2$  statistic (§3), which we minimize in order to find the most probable solution for a set of data in the framework of a specific model. In §4, we simulate observations of clusters with a specific density profile by mimicking real observations along with their errors, and demonstrate the ability to recover the correct (input) density profile from the projected quantities. We then try to fit a wrong model for the simulated system and show how we fail in doing so. In §5, we present the difficulties of the  $\beta$ -fit model to recover the right cluster parameters. In §6 we discuss future implications of this method and present our conclusions. We consider this paper as a simple, but necessary, first step towards lifting the line-of-sight degeneracy in galaxy clusters. We present the basic ideas here, postponing more detailed studies to later work.

## 2 MODEL POTENTIAL AND OBSERVABLES

We employ spherically symmetric cluster models and assume that the X-ray emitting intracluster gas is in hydrostatic equilibrium with the cluster gravitational potential. We assume that the gas is isothermal, and the mean molecular weight is constant throughout the cluster. These assumptions determine the density profile of the gas. In order to normalize the gas density, we fix the ratio between gas mass and dark mass within a given radius.

Then, specifying the three-dimensional cluster potential is sufficient to describe both the X-ray emission and the lensing properties of the cluster. Unfortunately, we do not know this three-dimensional potential *a priori*. Rather, we must elect a functional form for it, based on some additional

information, which can for instance be taken from numerical simulations.

There is growing evidence that the averaged radial structure of numerically simulated dark halos can well be described by a universal, two-parameter family of density profiles  $\rho(r)$ ,

$$\rho(r) = \frac{\rho_s}{x(1+x)^2}, \quad (1)$$

where  $x$  is the radius in units of a scale radius  $r_s$ . This shape of the density profile results independently of the parameters of the background cosmological model, and for halos with a broad range of masses (Navarro, Frenk, & White 1996; Cole & Lacey 1996; Huss, Jain, & Steinmetz 1997). On the observational side, Carlberg *et al.* (1997) have shown that the velocity dispersion profiles of observed clusters are compatible with density profiles of the form (1). If the X-ray emitting gas is isothermal and in hydrostatic equilibrium with the dark-matter profile (1), its flux profile has a flat core despite the cusp in the density profile. Density profiles with small core radii or central singularities better fit the observations of giant arcs. The latter require cluster density profiles with much smaller cores than inferred from X-ray observations (see *e.g.* Narayan & Bartelmann 1997 for a review).

If the gravitational potential of the density distribution (1) is normalized such that  $\Phi \rightarrow 0$  for  $x \rightarrow \infty$ , it can be written

$$\Phi(r) = -4\pi G \rho_s r_s^2 \frac{\ln(1+x)}{x}. \quad (2)$$

We replace the parameter  $\rho_s$  by the virial mass, by which we mean the mass contained within the radius  $r_{200}$  which encloses an average overdensity of  $\delta_c = 200^{\ddagger}$ . Since the mass within radius  $r$  is

$$M(r) = 4\pi \rho_s r_s^3 \left[ \ln(1+x) - \frac{x}{1+x} \right], \quad (3)$$

$r_{200}$  is determined by

$$\frac{3\rho_s}{c^3} \left[ \ln(1+c) - \frac{c}{1+c} \right] = 200 \bar{\rho}, \quad (4)$$

where  $\bar{\rho}$  is the mean cosmic density, and  $c = r_{200} r_s^{-1}$  is a concentration parameter.

An alternative source of information for the functional form of the potential could be derived from the observed projected X-ray flux profile. This leads to the famous derivation of the  $\beta$ -fit. We discuss the comparison between the adequacy of the two different functional forms later in §5.

## 2.1 X-ray Emission

An isothermal gas in hydrostatic equilibrium with a potential  $\Phi$  has a gas density of

$$\rho_{\text{gas}}(r) = \rho_{\text{gas},0} \exp[-(\tilde{\Phi}(r) - \tilde{\Phi}_0)], \quad (5)$$

where the index ‘0’ refers to some fiducial radius  $r_0$ .  $\tilde{\Phi}$  is the potential in units of the square of a fiducial velocity  $v_{\text{th}}$  of the gas particles,

<sup>‡</sup> This choice of  $\delta_c$  can be viewed as merely a change of variables. The actual value for the overdensity within the virialized region may change as function of the background cosmology, and is of no particular importance here.

$$\tilde{\Phi}(r) = v_{\text{th}}^{-2} \Phi(r) = \frac{\bar{m}}{kT} \Phi(r), \quad (6)$$

$\bar{m}$  being the mean mass per particle. For a mixture of 75% hydrogen and 25% helium (by mass), which we henceforth adopt,  $\bar{m} \simeq 10^{-24}$  g. For  $r_0$ , we choose the virial radius,  $r_{200}$ . We further adapt  $\rho_{\text{gas},0}$  such that the total gas mass within the virial radius is a fraction  $f_{\text{gas}}$  (hereafter called “gas fraction”) of the total mass,

$$\begin{aligned} 4\pi \int_0^{r_{200}} r^2 dr \rho_{\text{gas}}(r) &= f_{\text{gas}} M(r_{200}) \\ &= f_{\text{gas}} \frac{4\pi}{3} r_{200}^3 200 \bar{\rho}, \end{aligned} \quad (7)$$

where the last equality follows from the definition of  $r_{200}$ .

The emissivity of the gas due to thermal *bremsstrahlung* at position  $\vec{x}$  in the energy range  $E_a \leq E \leq E_b$  is

$$\begin{aligned} j_X(\vec{x}; E_a, E_b) &= 5.53 \times 10^{-24} \text{ erg cm}^{-3} \text{ s}^{-1} \\ &\times \left( \frac{kT}{\text{keV}} \right)^{1/2} \left( \frac{n_e}{\text{cm}^{-3}} \right)^2 \\ &\times \left[ \exp\left(-\frac{E_a}{kT}\right) - \exp\left(-\frac{E_b}{kT}\right) \right]. \end{aligned} \quad (8)$$

Assuming complete ionization, the electron density is  $n_e = 0.52 \bar{m}^{-1} \rho_{\text{gas}}$ . The flux  $S_X(\vec{\xi})$  received from the two-dimensional position  $\vec{\xi}$  within the cluster is the line-of-sight integral

$$S_X(\vec{\xi}; E_a, E_b) = \frac{1}{4\pi(1+z)^3} \int dl j_X(\vec{\xi}; l; E'_a, E'_b), \quad (9)$$

where the factor  $(1+z)^3$  accounts for redshifting the photons and for the ratio between luminosity distance and angular-diameter distance, and  $E'_{a,b} = (1+z)E_{a,b}$ . In real observations,  $S_X(\vec{\xi}; E_a, E_b)$  is further convolved with the detector response function. The flux can then be converted to photon numbers by means of the *bremsstrahlung* spectrum, the detector area, and the exposure time. Likewise, the observed photon spectrum is determined by the number of photons per energy bin  $[E_i, E_{i+1}]$ ,  $E_a \leq E_i \leq E_b$ .

## 2.2 Gravitational Lensing

The gravitational lensing effects of the density profile (1) have been calculated elsewhere (Bartelmann 1996). Given the potential (2), the effective lensing potential is

$$\psi = \frac{D_{\text{ds}}}{D_{\text{d}} D_{\text{s}}} \frac{2}{c^2} \int dl \Phi, \quad (10)$$

where  $D_{\text{d}}$ ,  $D_{\text{s}}$ , and  $D_{\text{ds}}$  are the angular-diameter distances from the observer to the cluster, to the sources, and from the cluster to the sources, respectively. The lensing convergence  $\kappa$  and shear components  $\gamma_{1,2}$  are then

$$\begin{aligned} \kappa &= \frac{1}{2}(\psi_{,11} + \psi_{,22}) \\ \gamma_1 &= \frac{1}{2}(\psi_{,11} - \psi_{,22}) \quad , \quad \gamma_2 = \psi_{,12} \end{aligned} \quad (11)$$

where indices  $i$  preceded by a comma denote partial derivatives with respect to  $x_i$ . The lensing properties of mass profiles of the form (1) have been worked out by Bartelmann (1996).

Gravitational lensing leads to coherent distortions of the images of background galaxies. Image ellipticities, which

can be quantified by, e.g., the quadrupole tensor of their surface brightness distribution, measure the two-component reduced shear

$$g_i = \frac{\gamma_i}{1 - \kappa} . \quad (12)$$

If the lens has a critical curve, an ambiguity arises in the  $g_i$  because of the parity change upon crossing the critical curve. An unambiguous measure of the ellipticity is then provided by the distortion  $\delta_i$ ,

$$\delta_i = \frac{2g_i}{1 + g_1^2 + g_2^2} . \quad (13)$$

Since galaxies do not usually appear circular,  $\delta$  cannot be inferred from individual galaxies, but must be determined statistically by averaging over a sufficient number of galaxy images. The assumption underlying this inference is that the intrinsic *orientations* of the galaxies is random. The measured galaxy ellipticities (to be related to the  $g_i$ ) are given by

$$\epsilon_1 + i\epsilon_2 = \frac{a-b}{a+b} \exp(2i\varphi) \quad (14)$$

with  $a$  and  $b$  the major and minor axes of the ellipse, respectively, and  $\varphi$  its orientation (position angle). The unlensed observed ellipticities follow the two-dimensional distribution

$$p_e(\epsilon_1, \epsilon_2) = \frac{\exp(-|\epsilon|^2 \sigma_\epsilon^{-2})}{\pi \sigma_\epsilon^2 [1 - \exp(-\sigma_\epsilon^{-2})]} , \quad (15)$$

with  $\sigma_\epsilon \sim 0.15$  (e.g. Miralda-Escudé 1991; Tyson & Seitzer 1988; Brainerd, Blandford, & Smail 1996). An iterative procedure to derive  $\delta$  from galaxy ellipticities has been described by Seitz & Schneider (1995).

Deep observations (e.g. Smail *et al.* 1995) find galaxy surface number densities of  $\sim 40 - 50 \text{ arcmin}^{-2}$  down to a magnitude limit of  $R \sim 25$ . According to Lilly *et al.* (1995), the average redshifts of such sources fall within  $0.8 - 1$ . If we want to average over  $\sim 10$  galaxies for each local estimate of the distortion, the intrinsic resolution limit for any such distortion map is  $\sim 30''$ . The uncertainty in the local determination of  $\delta$  can be estimated by the variance of the  $N'$  galaxy ellipticities used to determine  $\delta$ , divided by  $(N' - 1)^{1/2}$ .

### 3 COMBINED $\chi^2$ FUNCTION

What question can we answer by calling statistics to our assistance? We do not know *a priori* whether a certain model provides a good description to the data. We can, however, find answers to the three following questions:

- (i) Given the data, what are the best parameters to describe them, *in the framework of a specific model*?
- (ii) For these best parameters found earlier, how likely is the model, given the data?
- (iii) Given the data, which of  $n$  competing models is the most likely?

The first answer is provided by the  $\chi^2$  minimization, the second by the goodness-of-fit (GoF) evaluation, and the third by comparing GoF values as obtained for the  $n$  different models. By “model” we mean a functional parameterization of the three-dimensional gravitational potential of the system under consideration.

The ability to answer the aforementioned three questions is pending on our ability to constitute a decent  $\chi^2$  statistic. The  $\chi^2$  statistic can be easily interpreted if the error estimate is accurate, and the error distribution is Gaussian or close to Gaussian.

Our analysis makes use of the different sensitivity of the observables to the potential parameters. The  $\chi^2$  statistic should therefore take into account all observables simultaneously. For the clarity of presentation, however, we present the various terms in the statistic separately and combine them later.

#### 3.1 The Temperature Term: $\chi_T^2$

The first term in the  $\chi^2$  statistic deals with the emission-weighted temperature (“temperature” hereafter). In §2.1 we described the photon counts in the  $N_E$  photon energy bins from which the temperature is estimated. The assumption of cylindrical symmetry, the independence of temperature on projected radius due to the assumption of isothermality, and the poor spatial resolution of the observations lead us to consider only one annulus, centered on the X-ray flux centroid, for the temperature evaluation.

The overall number of photons is taken into account elsewhere (the flux term, see §3.2), and we must avoid taking it into account twice, or otherwise the terms would not be independent. We therefore normalize the photon number in each energy bin by the total observed number of photons in all energy bins.

In normalized units, the temperature term of the  $\chi^2$  statistic is

$$\chi_T^2 = \sum_{i=1}^{N_E} \frac{[n_\gamma^i - n_\gamma(E_i)]^2}{(\sigma_T^i)^2} . \quad (16)$$

The normalized photon count in energy bin  $E_i$  is  $n_\gamma^i$ . Given the model temperature and assuming *bremsstrahlung* radiation, the model for the cluster and the X-ray background predicts  $n_\gamma(E_i)$  photons in the same bin<sup>§</sup>. The error in the denominator has two contributions that add up in quadrature:  $\sigma_T^2 = \sigma_{T,1}^2 + \sigma_{T,2}^2$ . The two kinds of measurement error are the instrumental error and the background radiation that has to be estimated in each frequency bin. These errors are identical for all models, since we do not consider different X-ray background radiation models. We assume the average X-ray background radiation signal is known, so there is no explicit DC offset of the photon number counts. Fluctuations in the background, though, should still be taken into account. A gross approximation for the contributions of these two terms can be the square root of the number of observed photons, if the observational errors are all due to Poisson noise. We thus have

$$(\sigma_{T,1}^i)^2 + (\sigma_{T,2}^i)^2 \simeq n_\gamma^i . \quad (17)$$

Recall that here, too, we normalize by the overall number of *observed* photons. One has to stay away from very low photon number counts, where the result is biased by the

<sup>§</sup> When more than one annulus is taken into account, the l.o.s. integration with the relevant emission weighting must be carried out as well and added to  $\chi_T^2$ .

lower limit of detecting no photons at all, and the error symmetry breaks down.

If a model assumes more than one cluster, with different temperatures, one cannot avoid the integration needed to calculate the weighted sum that yields the expected projected temperature.

Note that longer integration time can reduce the relative importance of  $\sigma_{T,1}$ , but cannot help reduce the relative importance of the background radiation noise ( $\sigma_{T,2}$ ) as long as it is not due to a short temporal variation.

### 3.2 The Flux Term: $\chi_S^2$

The  $\chi^2$  term for the flux is similar to the term for the temperature. In both cases the data is the number of photons. Two distinct differences exist between the two: In the flux term, the independent data are numbers of photons in spatial pixels, and the important measure is the actual number, so it can not be normalized by the total number observed.

For  $N_p$  pixels, with the  $i^{\text{th}}$  pixel centered on  $\vec{\xi}_i$ ,  $N_\gamma^i$  measured photons in the pixel, and  $N_\gamma(\vec{\xi}_i)$  photons expected from the model, the flux  $\chi^2$  term is written as

$$\chi_S^2 = \sum_{i=1}^{N_p} \frac{[N_\gamma^i - N_\gamma(\vec{\xi}_i)]^2}{(\sigma_S^i)^2}. \quad (18)$$

Similarly to the  $\sigma_T$  calculation, here too we have the same two contributions which we can approximate by  $(\sigma_S^i)^2 \simeq N_\gamma^i$ . In the case of the flux, we are interested in both the absolute number of photons and their spatial distribution in the projected two-dimensional map as a function of  $\vec{\xi}_i$ .

### 3.3 The Ellipticity Term: $\chi_\delta^2$

The data “unit” for the shear field, as explained in §2.2, is an area of typically  $0.2 \text{ arcmin}^2$  in which there are enough background galaxies ( $\sim 10$ ) to average over, for deriving the mean reduced distortion (*cf.* eq. 13) in this area element ( $\langle \vec{\delta} \rangle$ ). The error in the derived distortion in each bin is model independent and can be calculated either by the dispersion about the average distortion in a given area, or by taking a non-lensed region, deriving the intrinsic ellipticity distribution for the same galaxy population, and dividing by the square root of the number of galaxies in each bin. The two methods give similar results of  $\sigma_\delta \sim 0.03$ . Since the area element sizes are identical across the cluster, so is the error for the average ellipticity values. The  $\chi^2$  term for the ellipticities is readily written

$$\chi_\delta^2 = \sum_{i=1}^{N_\delta} \frac{[\langle \vec{\delta} \rangle_i - \langle \vec{\delta}(\vec{\xi}_i) \rangle]^2}{\sigma_\delta^2}, \quad (19)$$

where, as usual,  $\langle \vec{\delta}(\vec{\xi}_i) \rangle$  is the distortion expected from the model about the position  $\vec{\xi}_i$ . The sum is over all regions,  $i$ , for which the ellipticity is evaluated ( $N_\delta$  regions altogether).

### 3.4 The Combined $\chi^2$

As stated earlier, the idea is to search for  $\chi^2$  minima in the potential parameter space, using all observables simultaneously. Say we have specified a functional form for the

potential  $\Phi(\vec{r})$  that involves only two fitting parameters, plus one parameter for the gas fraction. The X-ray temperature, the X-ray flux, and the distortion field in any bin, are all functionals of this potential. They can all be combined to result in one (complicated, non-linear) function. So can the data be combined. The overall  $\chi^2$  statistic has therefore  $N_E + N_p + N_\delta - 3$  degrees of freedom (d.o.f.), and is simply the sum

$$\chi^2 = \chi_T^2 + \chi_S^2 + \chi_\delta^2. \quad (20)$$

Notice that the number of d.o.f. for this function is *not* the sum of the number of d.o.f. when each individual term is considered separately.

Different models may have different numbers of fitting parameters [e.g. two spherical symmetric clusters along the l.o.s. may be specified by five or six (depending on the universality of  $f_{\text{gas}}$ ) plus the separation between the two clusters]. A fair comparison between models must include this simple fact.

The  $\chi^2$  minimization leaves us with a  $\chi_{\text{min}}^2$  for each model, and an estimate of the best fitting parameters for this model. In order to assess to what extent a specific model provides an adequate description for the data, the GoF is calculated according to

$$G = \Gamma\left(\frac{N_{\text{dof}}}{2}, \frac{\chi_{\text{min}}^2}{2}\right), \quad (21)$$

with  $\Gamma$  the incomplete gamma function. The GoF interpretation rests on two assumptions: (i) that the data that went into the  $\chi^2$  calculation are independent (so that the d.o.f. calculation truly represents the d.o.f. of the data and the model), and (ii) that the errors are distributed in a Gaussian fashion and uncorrelated. Validation of the second assumption can be carried out by inspection of the residuals distribution. If errors are indeed all due to a Poissonian process in the data collection, we have reasons to believe that by the central limit theorem, the errors are Gaussian. The prudent policy of taking large bins (in the relevant context for each observable), pays off by producing minimally correlated errors and independent processed data points.

## 4 DEMONSTRATION BY SIMULATIONS

### 4.1 Model Specification

We can now proceed and apply our technique to idealized test cases. We consider two such cases: either one isolated cluster, or two clusters projected onto each other along the line-of-sight. In the first case, all observables are completely specified by three parameters, viz. the two parameters of the dark-matter profile, for which we take the virial mass  $M_{\text{vir}}$  and the scale radius  $r_s$ , and the gas fraction,  $f_{\text{gas}}$  (by weight) within the virial radius.

Assuming that the gas fraction is “universal”, we have five parameters to describe two clusters, plus their mutual distance. If the clusters are sufficiently distant such that their gas distributions do not significantly overlap, their exact separation does not matter. This applies once they are separated by more than about the sum of their scale radii. If they are so close to each other that they are in the process of merging, their gas distributions become more complicated,

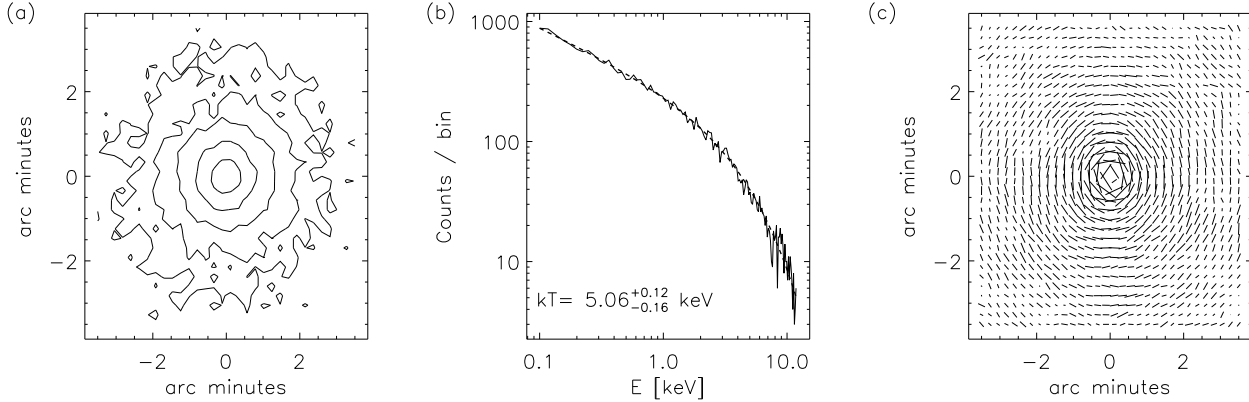


**Figure 1.** Examples for the simulated data we use. Panel (a): Simulated X-ray flux map. The contours are spaced by a factor of  $10^{1/2}$  in units of counts per pixel. The pixel size is  $13'' \times 13''$ , the field size is  $7' \times 7'$  (the field has  $32 \times 32$  pixels). Panel (b): Simulated X-ray spectrum, overlaid with a fit to the *bremsstrahlung* spectrum (dashed curve). The best-fit temperature is given in the plot, together with its  $1\sigma$  error. Panel (c): Distortion map produced from simulated background galaxy ellipticities. The same potential was used as for the X-ray data in the other panels. The length of the lines indicates the modulus of  $\delta$ , their orientation shows the direction of  $\delta$ .

especially because shocks form, hydrostatic equilibrium does not apply, and their dark-matter distributions are deformed. We assume here that the two clusters are sufficiently well separated such that their gas distributions do not interact, and then five parameters suffice to characterize their X-ray and lensing properties.

We consider simulated clusters at a redshift of  $z_c = 0.2$ , with a gas fraction of  $f_{\text{gas}} = 10\%$ , scale radii of  $r_s = 0.25 h^{-1} \text{ Mpc}$ , and a total virial mass of  $M_{\text{vir}} = 10^{15} M_{\odot}$ . When there are two clusters, this is the sum of the individual virial masses. The lensed sources are put at a redshift of  $z_s = 1$ .

We choose energy bins such as to mimic the energy resolution of the ASCA SIS (Tanaka, Inoue, & Holt 1994),

$$\frac{\Delta E}{E} = 0.02 \left( \frac{E}{5.9 \text{ keV}} \right)^{-1/2}, \quad (22)$$

which results in  $N_E = 121$  energy bins between  $E_a = 0.1 \text{ keV}$  and  $E_b = 12 \text{ keV}$ . The energy dependence of the effective detector area is modeled like that of the ROSAT HRI. The spectral energy distribution yields the emission-weighted temperature, which equals  $T$  for isothermal gas in a single cluster, or in a double cluster where both components have equal mass. For the noise in the photon counts, we use Poisson noise plus an additional background, for which we choose a DC level of  $3 \times 10^{-4} \text{ s}^{-1} \text{ arcmin}^{-2}$ , and a Gaussian distribution of the variation about this level with the standard deviation of  $\sigma_{S,2} = N_b^{1/2}$ , with  $N_b$  the number of background photons per exposure. This is in approximate agreement with the background noise in the ROSAT PSPC (Snowden *et al.* 1995). We ignore any energy dependence of the X-ray background. An example for a flux map and a spectrum simulated this way is shown in panels (a) and (b) of Fig. 1. Throughout, we have assumed an exposure time of 10 ksec.

For the background galaxies, we choose a surface number density of  $40 \text{ arcmin}^{-2}$  at a redshift of  $z_s = 1$ . Their positions are random, and their unlensed ellipticities are drawn from the two-dimensional distribution of eq. (15) with  $\sigma_e = 0.15$ . The galaxies are then distorted by the lensing ef-

**Table 1.** Parameters obtained from fitting a single cluster with a single cluster.  $M_{\text{vir}}$  is the virial mass,  $r_s$  is the scale radius,  $f_{\text{gas}}$  is the gas fraction, and  $G$  is the goodness-of-fit according to eq. (21).  $3\sigma$  errors are given. On the whole, the input parameters are well recovered, and lie all within the  $1\sigma$  contour level of the minimization.

	Parameter			
	$M_{\text{vir}}$ [ $10^{14} M_{\odot}$ ]	$r_s$ [ $h^{-1} \text{ Mpc}$ ]	$f_{\text{gas}}$ [%]	$G$ [%]
input	10.0	0.250	10.0	–
best fit	$10.0 \pm 0.3$	$0.250 \pm 0.004$	$10.0 \pm 0.3$	48.4

fect of the simulated clusters, and the distortion  $\delta$  is determined using the iterative algorithm provided by Schneider & Seitz (1995). An example for the distortion map  $\delta$  created by the lensing effect of the cluster whose X-ray emission is shown in panels (a) and (b) of Fig. 1, is displayed in panel (c) of the same figure.

## 4.2 Single-cluster case

We begin with “observations” created from a single cluster, and try to fit them with a model of the same functional form as used in the simulation, consisting of a single cluster. The best-fit parameters and the goodness-of-fit  $G$  at the minimum  $\chi^2$  are given in Tab. 1. The  $\chi^2$  per degree of freedom in this case is 1.001 which, for the number of degrees of freedom we have ( $N_{\text{dof}} = 2 \times 1024 + 121 - 3 = 2166$ ), yields a goodness-of-fit of  $G = 48.4\%$ . Examples with different realizations of the synthetic data show that these results are typical. As the table shows, the input cluster parameters are well reproduced.  $\chi^2$  contours in the  $M_{\text{vir}}-r_s$  and the  $M_{\text{vir}}-f_{\text{gas}}$  planes are shown in Fig. 2.

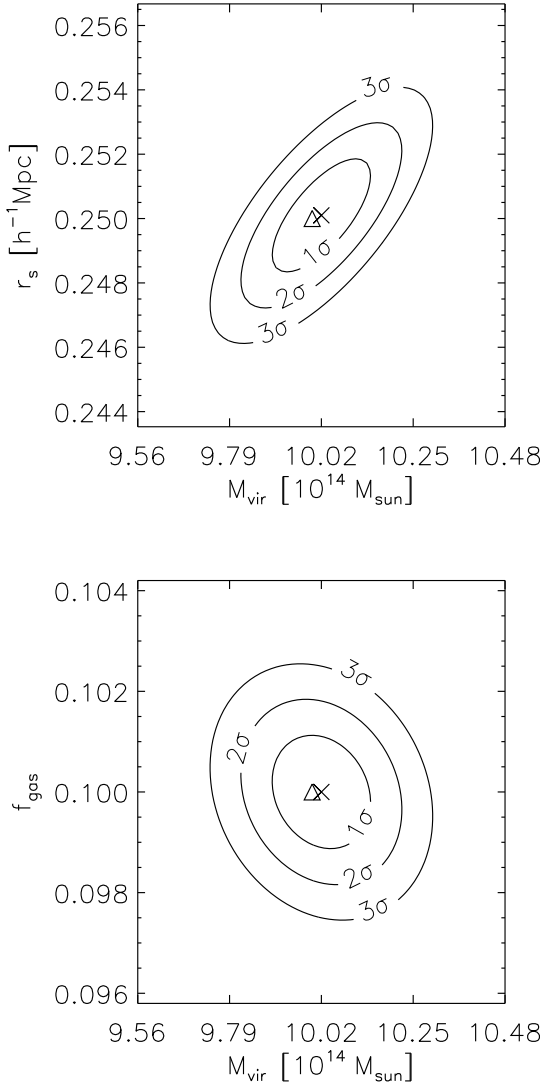


**Figure 2.** Cuts through the parameter space for fitting synthetic observations simulated with one cluster. The parameters are the virial mass  $M_{\text{vir}}$ , the scale radius  $r_s$ , and the gas fraction within the virial radius  $f_{\text{gas}}$ . Upper panel:  $\chi^2$  contours in the  $M_{\text{vir}}-r_s$  plane; lower panel:  $\chi^2$  contours in the  $M_{\text{vir}}-f_{\text{gas}}$  plane. The contours are  $1\sigma$ ,  $2\sigma$ , and  $3\sigma$  confidence levels. The cross marks the best-fit parameters, the triangle the parameters of the input model.

### 4.3 Double-cluster case

We now proceed to “observations” simulated with two clusters, with virial masses  $M_{\text{vir},1} = (1 - m)(M_{\text{vir},1} + M_{\text{vir},2})$  and  $M_{\text{vir},2} = m(M_{\text{vir},1} + M_{\text{vir},2})$ , projected onto each other along the line-of-sight. The first question is whether it is possible to significantly detect that the input cluster is double. This is the case if an attempt to fit the data with one cluster only results in a best-fit  $\chi^2$  which yields an unacceptable goodness-of-fit. We create synthetic data with two clusters, keeping the scale radii  $r_s = 0.25 h^{-1} \text{Mpc}$ , the gas fraction  $f_{\text{gas}} = 10\%$ , and the total cluster mass  $M_{\text{vir},1} + M_{\text{vir},2} = 10^{15} M_{\odot}$  constant. We then vary the mass

**Table 2.** Results from attempts at fitting with one cluster synthetic data that were simulated with two clusters. The input models consist of two clusters whose scale radii  $r_{s,1,2} = 0.25 h^{-1} \text{Mpc}$ , gas fraction  $f_{\text{gas}} = 10\%$ , and total mass  $M_{\text{vir},1} + M_{\text{vir},2} = 10^{15} M_{\odot}$  are kept constant, while their mass ratio  $m = M_{\text{vir},1}/M_{\text{vir},2}$  is varied. The table shows the mass  $M_{\text{vir}}$ , scale radius  $r_s$ , and gas fraction  $f_{\text{gas}}$  of the best-fitting single-cluster model. The  $\chi^2$  is to be compared to the number of degrees of freedom,  $N_{\text{dof}} = 2166$ .  $G$  is the goodness-of-fit according to eq. (21).  $3\sigma$  errors are given.

$m$	Parameter			$\chi^2$	$G$
	$M_{\text{vir}}$ [ $10^{14} M_{\odot}$ ]	$r_s$ [ $h^{-1} \text{Mpc}$ ]	$f_{\text{gas}}$ [%]		
1:1	$13.0 \pm 0.2$	$0.275 \pm 0.002$	$6.8 \pm 0.1$	3129	$< 10^{-4}$
1:2	$12.9 \pm 0.1$	$0.271 \pm 0.001$	$7.0 \pm 0.1$	2868	$< 10^{-4}$
1:3	$12.6 \pm 0.1$	$0.268 \pm 0.001$	$7.4 \pm 0.1$	2634	$< 10^{-4}$
1:4	$12.4 \pm 0.2$	$0.266 \pm 0.003$	$7.7 \pm 0.2$	2504	$< 10^{-4}$
1:5	$11.7 \pm 0.1$	$0.265 \pm 0.001$	$8.3 \pm 0.1$	2481	$2 \times 10^{-4}$
1:6	$11.5 \pm 0.2$	$0.263 \pm 0.002$	$8.4 \pm 0.2$	2425	$7 \times 10^{-3}$

ratio  $m = M_{\text{vir},1}/M_{\text{vir},2}$ . We investigate the cases  $m = \{1:1, 1:2, \dots, 1:6\}$ . Typical results are summarized in Tab. 2. The table shows that for all mass ratios, the single-cluster models fail to interpret the data acceptably. In turn, this implies that we can significantly distinguish between single- and double-cluster cases even if the mass ratio is fairly large.

Since for large  $N_{\text{dof}}$ , the  $\chi^2$  distribution approaches a Gaussian with mean  $N_{\text{dof}} = 2166$  and variance  $\sigma_{\chi^2} = (2 N_{\text{dof}})^{1/2} \approx 65.8$ , the formal significance for rejecting the single-cluster hypothesis is  $\sim 15 \sigma_{\chi^2}$  for  $m = 1:1$ , and  $\sim 4 \sigma_{\chi^2}$  for  $m = 1:6$ .

The expected trend is noticed, as for  $m \rightarrow 0$  the minimization should converge to the single cluster result. By further examination of the figures in the table we notice that the total mass of the system is always overestimated by about 10 – 30%, the scale radius is always overestimated by 5 – 10%, and the gas fraction is always underestimated by 15 – 30% (for these values of  $m$ ). The quoted errors do not thus represent the true errors, because the systematic errors from assuming the wrong model are ignored. The interpretation of this deviation is as follows: the minimization routine “detects” too low a temperature for the amount of flux it “sees”. It therefore tries to increase the amount of flux without changing the temperature, by widening the potential well (*i.e.* increasing  $r_s$ ) without making the well substantially deeper or equivalently without creating an unacceptable mismatch with the lensing distortion. This in turn ends up in attributing higher enclosed mass and a bit too high flux rate. The cure for the latter is achieved by the reduction of  $f_{\text{gas}}$ . This explains the false parameters we get out of the minimization.

Having seen that we can significantly reject the hypothesis that the synthetic data were simulated with a single cluster, we should now ask whether we get an acceptable GoF for the double-cluster model. And furthermore, how well can we recover the parameters of the individual clusters? For that purpose, we use the same double-cluster data that were created earlier once again, and fit them with a double-cluster model. Table 3 summarizes the results. The number

**Table 3.** Results from fitting with a double-cluster model synthetic data that were simulated with two clusters.  $m$  is the mass ratio,  $M_{\text{vir},1,2}$  are the virial masses,  $r_{s,1,2}$  the scale radii,  $f_{\text{gas}}$  is the gas fraction (assumed to be the same in both clusters), and  $G$  is the goodness-of-fit from eq. (21).  $3\sigma$  errors are given. The input parameters are all well recovered. The errors are somewhat larger than in the single-cluster case.

	$m$	Parameter				$f_{\text{gas}}$ [%]	$G$ [%]
		$M_{\text{vir},1}$ [ $10^{14} M_{\odot}$ ]	$M_{\text{vir},2}$ [ $10^{14} M_{\odot}$ ]	$r_{s,1}$ [ $h^{-1}$ Mpc]	$r_{s,2}$ [ $h^{-1}$ Mpc]		
input	1:1	5.0	5.0	0.25	0.25	10.0	–
best fit	$1.0 \pm 0.4$	$5.0 \pm 1.4$	$5.0 \pm 1.4$	$0.25 \pm 0.02$	$0.25 \pm 0.02$	$10.1 \pm 0.3$	23.1
input	1:2	6.7	3.3	0.25	0.25	10.0	–
best fit	$0.49 \pm 0.09$	$6.7 \pm 0.6$	$3.3 \pm 0.5$	$0.25 \pm 0.01$	$0.25 \pm 0.01$	$10.0 \pm 0.3$	26.0
input	1:3	7.5	2.5	0.25	0.25	10.0	–
best fit	$0.33 \pm 0.04$	$7.5 \pm 0.3$	$2.6 \pm 0.3$	$0.251 \pm 0.002$	$0.251 \pm 0.003$	$10.0 \pm 0.2$	24.1
input	1:4	8.0	2.0	0.25	0.25	10.0	–
best fit	$0.26 \pm 0.03$	$8.0 \pm 0.3$	$2.1 \pm 0.2$	$0.251 \pm 0.003$	$0.250 \pm 0.004$	$10.0 \pm 0.2$	24.5
input	1:5	8.3	1.7	0.25	0.25	10.0	–
best fit	$0.22 \pm 0.02$	$8.4 \pm 0.2$	$1.8 \pm 0.2$	$0.251 \pm 0.002$	$0.250 \pm 0.002$	$10.0 \pm 0.2$	27.9
input	1:6	8.6	1.4	0.25	0.25	10.0	–
best fit	$0.17 \pm 0.01$	$8.6 \pm 0.1$	$1.5 \pm 0.1$	$0.251 \pm 0.002$	$0.249 \pm 0.002$	$10.0 \pm 0.2$	27.9

of degrees of freedom is now reduced by two,  $N_{\text{dof}} = 2164$ . The values of  $\chi^2/N_{\text{dof}}$  are now typically  $\sim 1.02$ , resulting in goodness-of-fit values of  $G \sim 25\%$ . The input parameters are all well recovered. The  $3\sigma$  errors are somewhat larger than in the case of one cluster. They are largest for mass ratio  $m = 1:1$ , namely  $\sim 28\%$  for  $M_{\text{vir}}$ ,  $\sim 8\%$  for  $r_s$ , and  $\sim 3\%$  for  $f_{\text{gas}}$ , and they decrease to a few percent for smaller mass ratios. For examples, we show in Fig. 3 two cuts through the parameter space of a double-cluster model with mass ratio  $m = 1:3$ . The upper panel shows  $\chi^2$  contours in the  $M_{\text{vir},1}-M_{\text{vir},2}$  plane, the lower panel shows  $\chi^2$  contours in the  $r_{s,1}-r_{s,2}$  plane. The fairly large elongation of the  $\chi^2$  ellipses in the former case illustrates the comparatively large uncertainty in the masses: within a fairly broad range, it is possible to increase or decrease one mass at the expense of the other.

We also ran simulations where the clusters had different scale radii,  $r_{s,1} \neq r_{s,2}$ . When the less massive cluster has a smaller scale radius, it is recovered less precisely, because it is masked by the larger  $r_s$  of the dominant, more massive cluster. Even then, the masses of the individual clusters are well recovered.

## 5 A COMPARISON TO $\beta$ FITS

The conventional way to interpret X-ray observations is to azimuthally average the flux map and fit the functional form

$$S_X(r) \propto \left[ 1 + \left( \frac{r}{r_c} \right)^2 \right]^{-3\beta/2+1/2} \quad (23)$$

to the resulting flux profile. Assuming that the X-ray emitting gas is isothermal and in hydrostatic equilibrium with a spherically symmetric gravitational potential, the total mass implied by eq. (23) is

$$M_\beta(r) = \frac{3\beta r kT}{G\bar{m}} \frac{x^2}{1+x^2}, \quad (24)$$

where  $x = r/r_c$ . We apply this technique to the flux map shown in Fig. 1. The model (23) provides an excellent fit to the flux profile, with  $\beta = 0.74$  and  $r_c = 74.9 h^{-1}$  kpc (*cf.* Fig. 4). At  $r_{\text{lim}} = 0.49 h^{-1}$  Mpc, the flux profile drops below the background noise. At that radius, the spectral temperature of  $T = (5.1 \pm 0.4)$  keV yields, together with the other parameters,  $M_\beta(r_{\text{lim}}) = (2.0 \pm 0.2) \times 10^{14} M_{\odot}$  ( $3\sigma$  errors). Given these results, we can further determine the gas fraction required to explain the total X-ray flux. At  $3\sigma$  confidence (only noise included), it turns out to be  $f'_{\text{gas}} = (18 \pm 1)\%$ .

The flux map in Fig. 1 was simulated using *two* clusters of  $M_{\text{vir},1} = 5 \times 10^{14} M_{\odot} = M_{\text{vir},2}$  and  $r_s = 0.25 h^{-1}$  Mpc, so that the total mass within the radius accessible to X-ray observations should be  $M_{\text{total}}(r_{\text{lim}}) = 4.26 \times 10^{14} M_{\odot}$ . The input gas fraction was  $f_{\text{gas}} = 10\%$ . Of course,  $f'_{\text{gas}}$  from the  $\beta$  fit is now the gas fraction within the observable radius  $r_{\text{lim}}$  rather than the virial radius  $r_{\text{vir}}$ , with  $r_{\text{lim}} \sim r_{\text{vir}}/3$ , hence the prime on  $f_{\text{gas}}$ . The gas fraction of the input model slightly depends on  $r$ . At  $r_{\text{lim}}$ , it is  $f'_{\text{gas}} = 9.2\%$  rather than  $10\%$ .  $f'_{\text{gas}}$  as obtained from the  $\beta$ -fit technique therefore overestimates the true gas fraction by a factor of  $\sim 1.8 - 2.1$ . Obviously, the estimates from the  $\beta$  fit differ substantially from the true values *despite* the  $\beta$  fit's being excellent and the gas being in hydrostatic equilibrium within each of the two clusters.

Part of the gross discrepancy between the true gas fraction and that inferred from the  $\beta$  fit comes from the fact that fitting the X-ray observations alone does not give any clue as to the structure of the cluster along the line-of-sight. Other contributions emerge from the attempt to rely on the X-ray data alone without appealing to the lensing data.

For a single-cluster model with  $M_{\text{vir}} = 10^{15} M_{\odot}$  instead of the two-cluster model with the same total mass and a



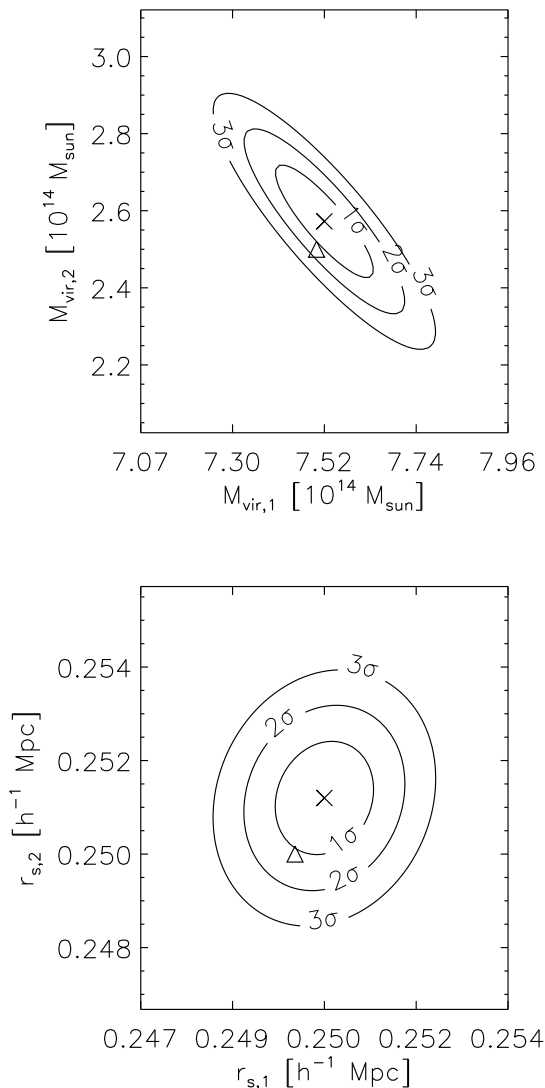


**Figure 3.** Two cuts through the parameter space for fitting synthetic observations simulated with two clusters. There are five parameters in total; the two virial masses  $M_{\text{vir},1,2}$ , the two scale radii  $r_{s,1,2}$ , and the gas fraction within the virial radius  $f_{\text{gas}}$  (assumed to be the same in both clusters). The mass ratio is  $m = 1:3$ . Upper panel:  $\chi^2$  contours in the  $M_{\text{vir},1}$ – $M_{\text{vir},2}$  plane; lower panel:  $\chi^2$  contours in the  $r_{s,1}$ – $r_{s,2}$  plane. The contours are for the same confidence levels as in Fig. 2. Crosses mark the best-fit parameters, triangles the input parameters.

mass ratio of  $m = 1:1$ , the  $\beta$ -fit mass is  $M_\beta(r_{\text{lim}}) = (3.6 \pm 0.4) \times 10^{14} M_\odot$ , while the true mass within  $r_{\text{lim}}$  is  $3.7 \times 10^{14} M_\odot$ . Therefore, in the single-cluster case, the  $\beta$ -fit mass is fairly accurate within the observable radius. The gross overestimate of the gas fraction in the double-cluster case is thus largely caused by the underestimate of the total mass.

In addition, the  $\beta$  fit profile (23) implies that the gas and dark matter density profiles flatten off at radii smaller than the core radius  $r_c$ . The true (input) dark matter density profile has a central cusp  $\propto r^{-1}$ . The isothermal gas density profile (5) approaches the center exponentially,  $\propto \exp(-Ax)$ . The actual central gas density is higher than deduced from

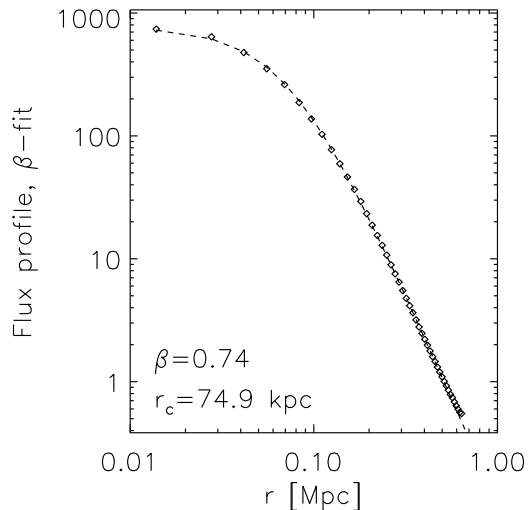


**Figure 4.** The azimuthally averaged flux profile (diamonds) of the cluster shown in Fig. 1, overlaid with a  $\beta$  fit profile (*cf.* eq. 23; dashed line). The parameters of the fit (the core radius  $r_c$  and  $\beta$ ) are given in the figure. At  $r_{\text{lim}} = 0.49 h^{-1}$  Mpc, the flux profile drops below the background level. The gas fraction within this radius, chosen such that the total cluster X-ray luminosity is reproduced, is  $f'_{\text{gas}} = (18 \pm 1)\%$ . The total mass within  $r_{\text{lim}}$ , implied by the  $\beta$ -fit parameters together with the temperature given in Fig. 1 and eq. (24), is  $M_\beta(r_{\text{lim}}) = (2.0 \pm 0.2) \times 10^{14} M_\odot$  ( $3\sigma$  errors).

(23), and therefore the actual total gas mass required to reproduce the observed X-ray flux is smaller than inferred. Even if we use the  $\beta$  model to interpret “observations” simulated with only one cluster, the best-fit gas fractions obtained are still systematically too high by  $\sim 20 - 40\%$ .

We also performed the counter experiment of simulating data with a King – (*i.e.*  $\beta = 1$ ) rather than the NFW profile, and fitting them with the NFW profile. In this case, the  $\beta$ -fit technique recovers the input parameters very well, including the gas fraction. When the core radius is small,  $r_c \lesssim 0.2 h^{-1}$  Mpc, the fit with the NFW profile fails. It yields a marginally acceptable goodness-of-fit of  $G = 8\%$  when the core radius is larger,  $r_c \gtrsim 0.25 h^{-1}$  Mpc. However, the best-fit mass is then  $M_{\text{vir}} = (11.4 \pm 0.5) \times 10^{14} M_\odot$  instead of the input  $M_{\text{vir}} = 10^{15} M_\odot$ .

## 6 SUMMARY AND OUTLOOK

Resolving the l.o.s. density profile of what appears to be a single cluster is not a hopeless task. In this paper, we have presented an approach that may ultimately lead to a clear distinction between different l.o.s. profiles. The key idea is to combine all the available information for the cluster, using simultaneously the X-ray data (their spatial and energy distribution), and the gravitational lensing properties of the cluster(s).

Two additional pieces of information were left out of the calculation. The first is the redshift distribution of cluster galaxies, because of the possible complication due to velocity bias that may interfere with the mass estimate, con-

tamination by non-member galaxies along the line-of-sight, and triple-valued zones. We precluded this information from the analysis even though it may help demonstrate the existence of a bimodal distribution in the case of two clusters. The second piece of information is the distribution of background galaxy sizes. This was left out because the intrinsic size distribution is broader than the ellipticity distribution, and consequently the additional constraints gained from including magnification effects are fairly weak.

We restricted our investigation to the question of how well a single cluster can be distinguished from two well separated clusters along the l.o.s. We have demonstrated, by using realistic simulations of cluster observations, that a single-cluster model for two clusters along the l.o.s. can be rejected, using the method, on a  $\sim 4 - 15\sigma$  level, depending on the mass ratio between the two clusters.

The true (input) parameters of the system, i.e. the total mass  $M_{\text{vir}}$  within a certain overdensity level, the scale radius  $r_s$ , and the gas content  $f_{\text{gas}}$ , can be recovered with typical ( $3\sigma$ ) fractional accuracies of a few percent for all parameters of single clusters. In the double-cluster case, the errors are largest when the mass ratio is close to unity, and they decrease to a few percent for smaller mass ratios. There is no good control over the separation between the clusters in the case of a two-cluster system.

We have further shown how wrong results for the cluster parameters can be obtained by using the  $\beta$ -fit that allegedly provides an appropriate fit for the X-ray flux data. Most of this effect can be ascribed to the fact that the  $\beta$ -fit technique is unable to recognize whether an apparent cluster is single or double. The method we propose in this paper does not suffer from that drawback, and hence we propose it supersedes the  $\beta$ -fit for mass and gas-fraction estimates.

We note that there is an increasing number of clusters for which there is evidence that they consist of two projected clusters rather than a of a single one. A well-known example for this is Abell 1689. Our choice of the singular NFW density profile is well motivated by numerical simulations (Navarro *et al.* 1996; Cole & Lacey 1996; Huss *et al.* 1997), and by observations which demonstrate that the mass profile derived from galaxy velocity data does not flatten off at small radii (Carlberg *et al.* 1997). In addition, strong gravitational lensing requires cluster cores to be much smaller than inferred from X-ray observations alone, if cores exist at all.

Reality spans a much broader range than what we examined in this paper. To begin with, two clusters along the l.o.s. can be in the process of merging. In that case hydrostatic equilibrium ceases to be a reasonable assumption and so does the isothermal model. Shocks due to the merging process heat the intracluster medium in an inhomogeneous fashion that is difficult to model. Hydrodynamic simulations of clusters may be useful in modeling the shock layer and its effect on the various X-ray observations.

Then, even for an isolated cluster which does not experience any merging, there may exist cooling flows that invalidate the assumption of isothermality (for the validity of hydrostatic equilibrium and isothermality in the presence of cooling flows, see *e.g.* Waxman & Miralda-Escudé 1995). There is hope these can be actually observed and may be azimuthally averaged over in order to regain the ability to model the cluster.

Another disturbing caveat may lie in the spherical symmetry we assume. Even though X-ray observations usually are circular on the sky for clusters (and not elliptical), this may be partially attributed to selection effects. Optically defined clusters show much more pronounced two-dimensional elliptical shapes in the galaxy distribution (*e.g.* Plionis, Barrow, & Frenk 1991). Although the ellipticity of the potential is smaller than that of the mass distribution, some of it must remain. A natural generalization of the current work would be to investigate families of elliptical potentials (Bartelmann & Kolatt 1997). By introducing the axis ratio as one of the free parameters, there is a continuous transition between spherical symmetry and elongated elliptical cluster when both are assumed to be in a hydrostatic equilibrium. Using the same  $\chi^2$  statistic as we used here, with this additional free parameter, should result in an estimate for the cluster elongation. In addition, mass models obtained from large arcs in some clusters can help constrain the morphology of the projected cluster mass distribution.

The removal of some of the projection effects by the means presented in this paper will allow a better understanding of the cluster environment and a safer use of clusters as large scale structure probes. These are two big leaps forward.

## ACKNOWLEDGMENTS

We thank M. Freyberg and S. Schindler for providing information on the ROSAT detectors, C. Canizares for advice, and Peter Schneider for a critical reading of the manuscript. This work was supported in part by the Sonderforschungsbereich 375 of the Deutsche Forschungsgemeinschaft (MB) and the US National Science Foundation (PHY-9507695; TK).

## REFERENCES

- Abell, G.O., 1958, ApJS, 3, 211
- Abell, G.O., Corwin Jr., H.G., Olwin, R.P., 1989, ApJS, 70, 1
- Bahcall, N.A., 1988, ARA&A, 26, 631
- Bahcall, N.A., Cen, R.Y., 1993, ApJ, 407, L49
- Bartelmann, M., 1996, A&A, 313, 697
- Bartelmann, M., Steinmetz, M., 1996, MNRAS, 283, 431
- Bartelmann, M., Kolatt, T.S., 1997, in preparation
- Brainerd, T.G., Blandford, R.D., Smail, I., 1996, ApJ, 466, 623
- Burns, J.O., Ledlow, M.J., Loken, C., Klypin, A., Voges, W., Bryan, G.L., Norman, M.L., White, R.A., 1996, ApJ, 467, L49
- Carlberg, R.G., Yee, H.K.C., Ellingson, E., Morris, S.L., Abraham, R., Gravel, P., Pritchet, C.J., Smecker-Hane, T., Hartwick, F.D.A., Hesser, J.E., Hutchings, J.B., Oke, J.B., 1997, preprint astro-ph/9703107
- Cavaliere, A., Fusco-Femiano, R., 1976, A&A, 49, 137
- Cole, S., Lacey, C., 1996, MNRAS, 281, 716
- Dalton, G.B., Efstathiou, G., Maddox, S.J., Sutherland, W.J., 1994, MNRAS, 269, 151
- Ebeling, H., Voges, W., Böhringer, H., Edge, A.C., Huchra, J.P., Briel, U.G., 1996, MNRAS, 281, 799
- Eke, V.R., Cole, S., Frenk, C.S., 1996, MNRAS, 282, 263
- Fadda, D., Girardi, M., Giuricin, G., Mardirossian, F., Mezzetti, M., 1996, ApJ, 473, 670
- Gioia, I.M., Maccacaro, T., Schild, R.E., Wolter, A., Stocke, J.T., Morris, S.L., Henry, J.P., 1990, ApJS, 72, 567

- van Haarlem, M.P., Frenk, C.S., White, S.D.M., 1997, preprint astro-ph/9701103, MNRAS, in press
- Holzzapfel, W.L., Arnaud, M., Ade, P.A.R., Church, S.E., Fischer, M.L., Mauskopf, P.D., Rephaeli, Y., Wilbanks, T.M., Lange, A.E., 1997, preprint astro-ph/9702224
- Huss, A., Jain, B., Steinmetz, M., 1997, preprint astro-ph/9703014
- Lilly, S.J., Tresse, L., Hammer, F., Crampton, D., Le Fèvre, O., 1995, ApJ, 455, 108
- Loeb, A., Mao, S., 1994, ApJ, 435, L109
- Mazure, A., Katgert, P., den Hartog, R., Biviano, A., Dubath, P., Escalera, E., Focardi, P., Gerbal, D., Giuricin, G., Jones, B., Le Fèvre, O., Moles, M., Perea, J., Rhee, G., 1996, A&A, 310, 31
- Miralda-Escudé, J., 1991, ApJ, 370, 1
- Miralda-Escudé, J., Babul, A., 1995, ApJ, 449, 18
- Navarro, J.F., Frenk, C.S., White, S.D.M., 1996, ApJ, 462, 563
- Plionis, M., Barrow, J.D., & Frenk, C.S. 1991, MNRAS, 249, 662
- Rephaeli, Y., 1995, ApJ, 445, 33
- Roettiger, K., Stone, J.M., Mushotzky, R., 1997, preprint astro-ph/9702072
- Schneider, P., Seitz, C., 1995, A&A, 294, 411
- Snowden, S.L., Freyberg, M.J., Plucinsky, P.P., Schmitt, J.H.M.M., Trümper, J., Voges, W., Edgar, R.J., McCammon, D., Sanders, W.T., 1995, ApJ, 454, 643
- Sunyaev, R.A. & Zel'dovich, Ya.B. 1980, ARA&A, 18, 237
- Tanaka, Y., Inoue, H., Holt, S.S., 1994, PASJ, 46, L37
- Tyson, J.A., Seitzer, P., 1988, ApJ, 335, 552
- Viana, P.T.P., Liddle, A.R., 1996, MNRAS, 281, 323
- Waxman, E., Miralda-Escudé, J., 1995, ApJ, 451, 451
- White, S.D.M., Efstathiou, G., Frenk, C.S., 1993, MNRAS, 262, 1023
- Zwicky, F., Herzog, E., Wild, P., Karpowicz, M., Kowal, C.T., 1968, Calif. Inst. for Technology, Pasadena